Research Square

Preprints are preliminary reports that have not undergone peer review.
They should not be considered conclusive, used to inform clinical practice,
or referenced by the media as validated information.

Limit-state geometry of trailing-edge tensile cracks in soil slopes with a tensile strength threshold

Jijie Du

dujj25@mail2.sysu.edu.cn

Sun Yat-Sen University

Liansheng Tang

eestls@mail.sysu.edu.cn

Guangzhou Institute of Science and Technology

Jianing Huang

Sun Yat-sen University

Zihua Cheng

Shenzhen Geological Science and Technology Innovation Center

Research Article

Keywords: Cemented soil slope, tensile strength, trailing-edge tensile crack, limit-state geometry

Posted Date: November 2nd, 2026

DOI: https://doi.org/10.21203/rs.3.rs-11544266/v1

License: This work is licensed under a Creative Commons Attribution 4.0 International License.
Read Full License

Additional Declarations: The authors declare no competing interests.

Limit-state geometry of trailing-edge tensile cracks in soil slopes with a tensile strength threshold

Jijie Du [b], Liansheng Tang [a,b,c,*], Jianing Huang [b], Zihua Cheng [d]

a. School of Architectural Engineering, Guangzhou Institute of Science and Technology, Guangzhou 510540, China

b. School of Earth Sciences and Engineering, Sun Yat-sen University, Zhuhai 519080, China

c. Southern Marine Science and Engineering Guangdong Laboratory (Zhuhai), Zhuhai 519082, China

d. Shenzhen Geological Science and Technology Innovation Center, Shenzhen 518000, Guangdong, China

[*] Corresponding author, E-mail: eestls@mail.sysu.edu.cn

Acknowledgments

The authors gratefully acknowledge Prof. John S. McCartney for his valuable comments and constructive suggestions, which helped improve the quality of this work. This work was supported by the National Natural Science Foundation of China (No. 42277142), the National Cultivation Project for Guangzhou Institute of Science and Technology (No. 2024gjp002), and the Research Start-up Funding Project for Guangzhou Institute of Science and Technology (No. 2023KYQ028).

CRediT authorship contribution statement

Jijie Du: Writing – original draft, Methodology, Conceptualization, Software. **Liansheng Tang:** Writing – review & editing, Supervision, Funding acquisition. **Jianing Huang:** Data curation, Visualization, Writing – original draft & editing. **Zihua Cheng:** Writing – review & editing, Software.

Declaration of competing interest

The authors declare that they have no known competing financial interests or personal relationships that could have appeared to influence the work reported in this paper.

Data availability

Data will be made available on request.

Abstract: Trailing-edge tensile cracks can contribute to tensile–shear slope failure. Many analytical models prescribe a vertical crack and solve only for depth, and tensile strength, σ_t, is also often neglected or treated indirectly. This study develops a limit-state formulation for an initially intact, homogeneous cemented soil slope under drained conditions. Shear resistance follows the Mohr–Coulomb criterion, while tensile failure is governed independently by σ_t. The formulation treats the limit-state crack depth L and inclination δ as coupled unknowns of the tensile–shear limit-state problem rather than prescribing the crack inclination in advance. The solution satisfies tensile and shear failure conditions, equilibrium, and geometric constraints. The formulation is examined using theoretical benchmarks, a bounded loess field comparison, and simulations using MatDEM. The benchmarks reproduce established depth trends. The field measurement falls within the calculated range for the adopted tensile-strength ratio. The simulations preserve the crack/no-crack distinction and show closer correspondence in inclination than in depth, with mean absolute differences of 4.22° and 1.66 m, respectively. Increasing σ_t reduces L and δ and may suppress a positive-depth solution. The cohesion intercept generally increases both, while unit weight mainly reduces L. Global Sobol analysis ranks cohesion > tensile strength > friction angle > unit weight for the zero-including depth response.

Keywords: Cemented soil slope; tensile strength; trailing-edge tensile crack; limit-state geometry;

1. Introduction

Slope failure is a major concern in geological hazard prevention and geotechnical engineering. It is often described as shear movement along a continuous sliding surface, yet field investigations, physical model tests, and numerical simulations show that shear deformation in the lower or frontal part of a slope is frequently accompanied by tensile cracking near the crest or trailing-edge (Dwiantara et al. 2023; He et al. 2022; Mukhlisin and Khiyon 2018). A trailing-edge tensile crack changes the continuity of the potential sliding mass and the local stress-transfer path, and it can provide a preferential pathway for rainfall infiltration and surface water (Jia et al. 2024; Ren et al. 2025; Sun et al. 2019; Zhang et al. 2012). Therefore, trailing-edge tensile cracks should not be viewed as isolated surface features; they form part of a tensile-shear failure mechanism. Their geometry is consequently important for understanding how tensile cracking interacts with subsequent shear deformation.

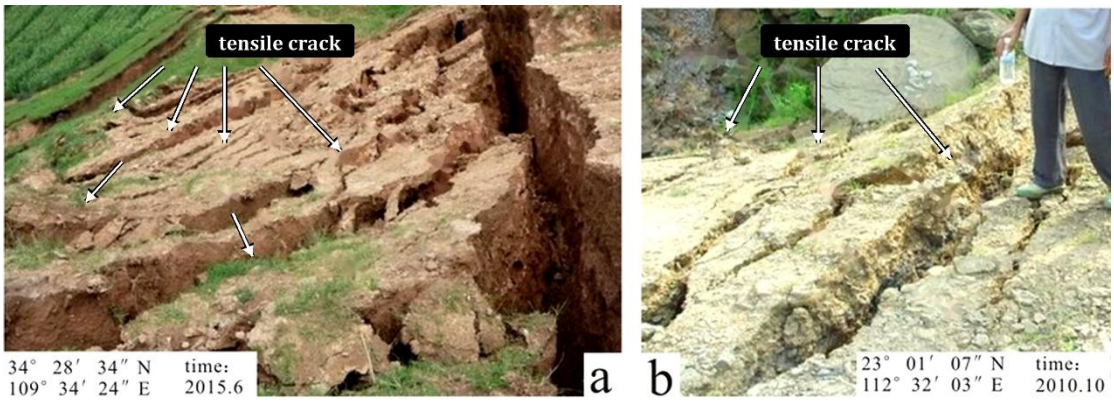


Fig. 1. Field examples of trailing-edge tensile cracks in soil slopes Tang et al. (2019).

The formation of a trailing-edge tensile crack is governed by the interaction between the local tensile stress state and the tensile strength of soil. Reduced lateral confinement and outward slope deformation can generate tensile stress near the trailing edge (Lu et al. 2022; Stockton et al. 2019; Tang et al. 2019). A trailing-edge tensile crack can initiate when the local tensile stress reaches the tensile strength threshold; thus, the stress state controls where tensile failure is possible, whereas tensile strength controls whether the failure condition is reached.

Existing studies of trailing-edge tensile cracks include physical model tests, numerical simulations, and theoretical analyses. Physical model tests directly record the development of deformation and cracking during slope failure (Deng et al. 2019; Fang et al. 2025; Miao et al. 2025; Yang et al. 2024; Yin et al. 2023). They provide important evidence on the sequence of tensile cracking and shear deformation, but the measured crack depth and inclination depend on model scale, boundary conditions, loading path, and the observation stage, so it is difficult to derive a general relationship between soil parameters and crack geometry from tests alone. Numerical simulations provide further information on stress redistribution, displacement localization, damage, and crack development (Hu et al. 2024; Sun et al. 2022; Xu et al. 2024; Yuan et al. 2020). Continuum methods describe stress and displacement fields, while discrete element methods represent particle bond breakage and connected damage paths. However, their results depend on constitutive assumptions, parameter calibration, and crack-identification criteria, and crack geometries are commonly extracted from calculated fields rather than obtained directly as solution variables. Among the geometric descriptors relevant to the present two-dimensional issue, crack depth and inclination are of particular interest. Experimental investigations and numerical simulations have demonstrated that trailing-edge tensile cracks do not necessarily develop as vertical planes; inclined crack geometries have been observed under different geological and mechanical conditions (Wang et al. 2022; Zhou et al. 2020). These observations indicate that inclination should be considered together with depth when characterizing trailing-edge tensile crack geometry.

Theoretical approaches provide an efficient and physically interpretable route for investigating trailing-edge tensile cracks with relatively limited computational effort.

Analytical solutions based on limit equilibrium and limit analysis methods have therefore been widely adopted to calculate trailing-edge tensile crack depth (Michalowski 2013; Utili 2013; Zhu et al. 2021). For example, Utili (2013) developed a kinematic limit analysis framework to investigate slopes with cracks and provided crack-depth solutions, while Michalowski (2013) considered crack formation mechanisms within a rigorous limit analysis framework. These analytical approaches provide convenient tools for parametric investigations and engineering assessment.

However, most existing analytical studies focus primarily on crack depth, whereas the inclination of the trailing-edge tensile crack is commonly prescribed in advance, typically as a vertical plane (Michalowski 2013; Taghavi et al. 2010; Utili 2013; Zhu et al. 2021). Such an assumption simplifies the formulation, but it fixes the trailing-edge tensile crack inclination before the mechanical conditions governing tensile failure are evaluated. The inclination of a trailing-edge tensile crack can modify the geometry of the potentially detached soil mass, the interaction between the trailing-edge tensile crack and the shear surface, thereby changing the geometric conditions relevant to subsequent slope-stability assessment (Venkat Ramana et al. 2023; Gao et al. 2015; Utili 2013). Therefore, an analytical formulation that determines inclination together with crack depth is required.

An additional limitation concerns how the tensile strength enters analytical formulations. Many existing formulations neglect tensile strength or introduce tensile effects indirectly through modified shear strength parameters, without explicitly representing the tensile failure criterion. Although some studies have incorporated tensile strength cut-off conditions into slope stability analyses, the coupled influence of tensile strength on crack depth and inclination of a trailing-edge tensile crack remains insufficiently understood. The distinction is not merely the addition of crack inclination as an extra output; rather, crack geometry is reformulated from a prescribed geometric condition into a set of coupled unknowns constrained simultaneously by tensile failure, shear failure, equilibrium, and geometric admissibility.

To address these limitations, this study develops a two-dimensional limit-state model for an initially intact, homogeneous cemented soil slope under drained conditions. Shear resistance follows the Mohr–Coulomb criterion. Tensile failure is governed independently by the tensile strength σ_t. The model represents a local tensile-shear wedge bounded by a trailing-edge tensile crack and a lower shear surface. The crack depth and inclination are treated as coupled unknowns and are determined simultaneously under the tensile-failure, shear-failure, equilibrium, and geometric admissibility constraints. The formulation is examined through theoretical benchmarks, a bounded field comparison, MatDEM simulations, and parametric and Sobol sensitivity analyses. The resulting framework provides a mechanically constrained basis for interpreting trailing-edge tensile crack geometry.

2. Constrained limit-state formulation for tensile crack geometry

2.1 Problem statement

The formulation considers a local, two-dimensional model in an initially intact, homogeneous cemented soil slope under drained conditions, with the shear response represented by the Mohr–Coulomb criterion (Fig. 2). The potential trailing-edge tensile crack is denoted by BF, and the lower shear surface by EF. Under the limit state, BF is characterized by the limit-state depth L and inclination δ. The prescribed inputs are the macroscopic strength parameters σ_t, c, and φ, together with unit weight γ. They refer to the prescribed material state.

The field photograph and interpreted longitudinal section in Figs. 2(a) and 2(b), adapted from Xian and Wei (2025), provide the visual basis for the idealized two-dimensional slope geometry in Fig. 2(c). The abstraction retains the principal slope profile, trailing-edge boundary and sliding surface required by the present formulation, rather than the site-specific hydrogeological processes.

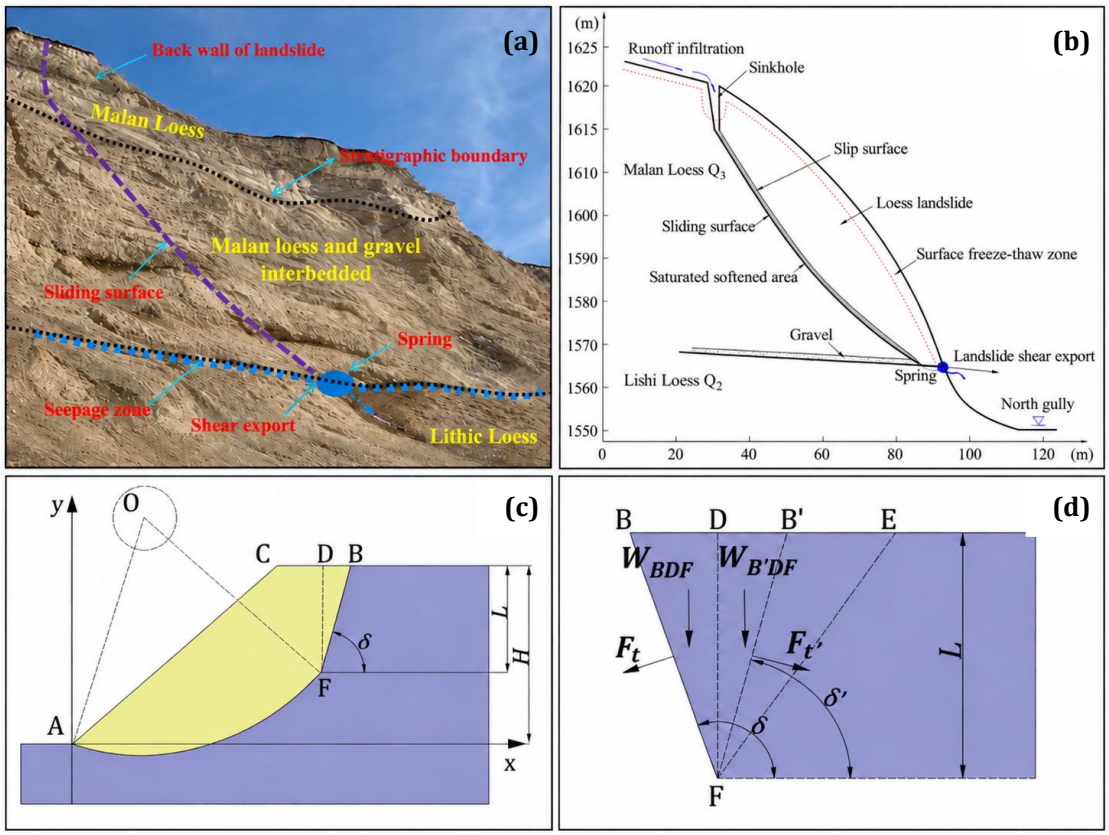


Fig. 2. Field basis and idealization of the trailing-edge tensile-crack geometry: (a) field view of the back wall; (b) interpreted longitudinal section; (c) idealized two-dimensional slope geometry; and (d) supplementary tensile-crack configuration. Panels (a) and (b) are adapted from Xian and Wei (2025).

Consistent with existing models (Michalowski 2013; Taghavi et al. 2010; Utili 2013; Zhang et al. 2018; Zhu et al. 2021), overall slope height and slope angle do not enter the governing equations independently. The formulation therefore does not quantify overall-slope

geometry effects, locate the physical trailing-edge tensile crack or its tip, or predict geometry at a particular deformation stage.

Configurations with $\delta > \pi/2$ are examined using the supplementary trailing-edge tensile-crack geometry in Fig. 2(d).

When the normal tensile stress on the potential trailing-edge tensile crack reaches σ_t, the corresponding tensile forces on BF and B′F are determined by the tensile strength criterion. Taking moments of point F for the two corresponding configurations gives:

$$L\gamma \cot^2 \delta + 3\sigma_t \csc^2 \delta = L\gamma \cot^2 \delta' + 3\sigma_t \csc^2 \delta' \tag{1}$$

where γ is the unit weight of soil and σ_t is the tensile strength of soil. According to the geometric relation $\delta' = \pi - \delta$, the assumed case $\delta > \pi/2$ corresponds to $0 < \delta' < \pi/2$. Eq. (1) indicates that the tensile-limit moment relationship of the $\delta > \pi/2$ configuration can be represented by the supplementary trailing-edge tensile crack B′F with $\delta' < \pi/2$. Therefore, an inclination δ larger than $\pi/2$ does not provide an additional independent trailing-edge tensile-crack mechanism in the present limit-equilibrium formulation. Combining this result with the geometric ordering gives the admissible domain $0 < \theta < \delta < \pi/2$.

2.2 Mechanical assumptions and governing constraints

Fig. 3 gives the corresponding mechanical model. Following the tensile–shear wedge framework of Zhu et al. (2021) and Zhang et al. (2018), the trailing-edge tensile crack and potential shear surface are considered jointly in force and moment equilibrium.

The forces acting on the triangle BEF includes its self-weight G, the shear force F_s on EF, the normal force F_n perpendicular to EF, and the tensile force F_t acting perpendicular to the trailing-edge tensile crack BF.

The model is founded upon the following fundamental assumptions:

(1) The system is treated as a plane-strain problem involving homogeneous, continuous cemented soil without internal fissures under drained conditions and gravity loading.

(2) The macroscopic shear resistance of soil is represented by the Mohr–Coulomb criterion, with c and φ denoting the drained cohesion intercept and friction angle, respectively. Tensile failure is governed independently by the macroscopic tensile strength σ_t. The parameters c, φ, and σ_t refer to the same prescribed material state.

(3) BF is treated as a straight potential trailing-edge tensile crack whose normal tensile stress reaches σ_t at the limit state.

(4) Triangle BEF is idealized as a rigid body with negligible internal deformation.

(5) EF is a potential shear failure plane satisfying a limit equilibrium.

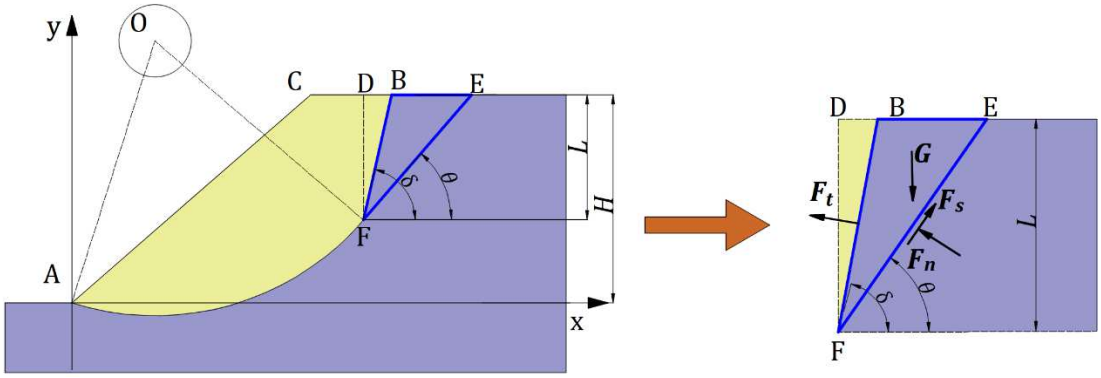


Fig. 3. Mechanical model of the trailing-edge tensile crack.

2.3 Solution for limit-state depth and inclination

2.3.1 Solution based on static forces equilibrium

The force resultants in Fig. 3 are:

$$\begin{cases} F_t = \sigma_t L / \sin\delta \\ F_s = F_n \tan\varphi + cL / \sin\theta \\ G = \left(\cot\theta - \cot\delta\right) L^2 \gamma / 2 \end{cases} \tag{2}$$

where σ_t, φ, c, and γ denote tensile strength (kPa), friction angle (°), cohesion intercept (kPa), and unit weight (kN/m^3), respectively. The strength parameters refer to the same prescribed material state. L is the limit-state depth (m), while δ and θ are the inclinations of BF and EF, respectively.

Force equilibrium gives:

$$\begin{cases} F_t \sin\delta + F_n \sin\theta = F_s \cos\theta \\ G = F_t \cos\delta + F_n \cos\theta + F_s \sin\theta \end{cases} \tag{3}$$

Substituting Eq. (2) into Eq. (3), the unknowns L and F_n can be obtained as follows:

$$\begin{cases} L = \dfrac{\csc\left(\delta-\theta\right)\csc\left(\theta-\varphi\right)K}{\gamma} \\ F_n = \dfrac{\cos\varphi\left(c\cot\theta - \sigma_t\right)\csc\left(\delta-\theta\right)\csc^2\left(\theta-\varphi\right)K}{\gamma} \end{cases} \tag{4}$$

where K is:

$$K = \sigma_t \cos\left(\delta+\varphi\right) - \sigma_t \cos\left(\delta - 2\theta + \varphi\right) + 2c\cos\varphi\sin\delta \tag{5}$$

Eqs. (4) and (5) give L for specified δ and θ. Because both angles remain unknown, they must be determined from the moment equilibrium conditions.

2.3.2 Solution based on moment equilibrium

Moment equilibrium of the rigid wedge gives Eq. (6).

$$\overrightarrow{M_{F_t}} + \overrightarrow{M_{F_n}} + \overrightarrow{M_{F_s}} + \overrightarrow{M_G} = 0 \tag{6}$$

where M_t, M_s, M_n and M_G are the moment vectors of F_t, F_s, F_n and G, respectively, about a

selected rotation point.

Normal compression on EF is expected to increase downward with overburden, but its exact distribution is unavailable in the simplified limit equilibrium framework. It is therefore approximated as linear (Fig. 4), with the resultant acting at one-third of the corresponding height from the lower end, analogous to a triangular pressure distribution. This is an equivalent resultant-force assumption rather than an exact stress integration or complete internal stress field solution.

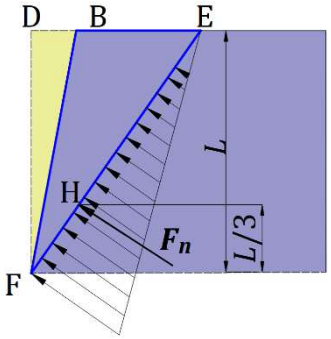


Fig. 4. Normal pressure on EF plane.

For F_s, the acting point is taken at the midpoint of EF. Because δ and θ are both unknown, moment equilibrium is considered using point F. The following expressions give the moment arms about point F used in the subsequent reduction.

$$\begin{cases} LF_{F_t} = L/(2\sin\delta) \\ LF_{F_n} = L/(3\sin\theta) \\ LF_G = L\left(\cot\delta + \cot\theta\right)/3 \end{cases} \tag{7}$$

where LF_{Ft}, LF_{Fn} and LF_G are the moment arms of F_t, F_s and G about point F. Substituting Eqs. (4) and (5) into Eqs. (2) and (7), and then into Eq. (6), gives Eq. (8).

$$\frac{\csc(\delta-\theta)\csc(\theta-\varphi)C_1C_2}{\gamma} = 0 \tag{8}$$

where C_1 and C_2 are:

$$C_1 = \cos\varphi\left(\sigma_t\cos 2\theta + 2c\sin 2\delta - \sigma_t\right) + \sigma_t\left(\sin 2\theta - 2\sin 2\delta\right)\sin\varphi \tag{9-1}$$

$$C_2 = c\cos\varphi\csc\theta - \sigma_t\csc\delta\sin\left(\delta-\theta+\varphi\right) \tag{9-2}$$

The parameters δ and θ must simultaneously satisfy Eq. (8) under the constraint $0 < \theta < \delta < \pi/2$. Exact closed-form expressions for δ and θ cannot be directly derived from these constraints. Therefore, the admissible (θ, δ) pairs are searched within the prescribed angular domain and substituted into Eq. (4). When multiple admissible trailing-edge tensile crack geometries satisfy the limit-equilibrium and tensile failure conditions, the minimum positive L is selected as the governing solution (Zhu et al. 2021), and the corresponding δ defines the inclination of the trailing-edge tensile crack. From a mechanical perspective, a smaller L represents a less extensive tensile failure geometry and therefore requires a lower level of

deformation-induced tensile development to satisfy the tensile strength threshold. Thus, the minimum positive solution corresponds to the most readily achievable admissible limit-state geometry within the proposed framework.

2.4 Hierarchical constrained solution procedure

Because the coupled angular variables do not admit an explicit closed-form solution, the constrained nonlinear system is solved using a hierarchical constrained search. The procedure explores the admissible (θ, δ) domain, evaluates the corresponding L, rejects candidates that violate physical or geometric constraints, and selects the minimum admissible L. Fig. 5 summarizes the general search logic; the numerical implementation used for the reported calculations is specified below.

First, the θ domain is discretized into a uniform coarse grid defined as:

$$\theta_i = \theta_{min} + i\Delta\theta_c, i = 1, 2, \ \ldots, \ N \tag{10}$$

where $\theta_{\min}$ and $\theta_{\max}$ denote the lower and upper numerical bounds. In the implementation used for the reported calculations, 600 uniformly spaced θ values are evaluated over $\theta \in [\max(0.3, \varphi + 10^{-7}), \pi/2 - 0.001]$. For each θ_i, the admissible inclination range satisfies $\theta_i < \delta < \pi/2 - 10^{-7}$. Eq. (11) gives the generic notation for the δ candidate set:

$$\delta_j = \theta_i + j\Delta\delta_j, \ j = 1, 2, \ldots, M \tag{11}$$

where $\Delta\delta$ denotes the nominal angular resolution. In the actual implementation, δ is not exhaustively scanned on a uniform grid. Instead, Eq. (8) is evaluated branch-wise by solving $C_1 = 0$ and $C_2 = 0$ to generate the admissible δ roots for each θ_i.

For each candidate pair (θ_i, δ_j), the limit-state depth L is computed using the limit equilibrium formulation based on Eqs. (4), (5), and (8):

$$L_{ij} = L\left(\theta_i, \delta_j, \sigma_t, c, \varphi, \gamma\right) \tag{12}$$

Candidates are screened for finite L with $L \geq 0$ and geometric admissibility. If more than one admissible δ root is returned for a given θ_i, all roots satisfying the geometric and physical admissibility constraints are retained. The corresponding L value is evaluated for each admissible root, and the minimum finite positive L is selected for that θ_i. Non-finite solutions and numerical outliers with $|L| \geq 10^6$ are discarded.

For each θ_i, the minimum admissible L is identified as:

$$L_i^* = \min\left(L_{ij}\right) \tag{13}$$

with corresponding δ_i^*.

A global comparison over all θ_i is then performed to determine the optimal solution:

$$\theta^* = argmin\left(L_i^*\right) \tag{14}$$

and the final trailing-edge tensile-crack geometry is given by $L = L(\theta, \delta)$. The governing result is therefore the global minimum positive L over the retained θ–δ candidates. A grid-

doubling check from 600 to 1200 θ points was additionally performed for representative parameter combinations spanning the baseline and parameter extremes; the resulting change was below 0.001% for L and below 0.021° for δ, indicating that the adopted θ resolution is sufficient for the reported results.

If no admissible finite positive-depth solution exists over the entire θ domain, the system is classified as a crack-suppression state. In this state, $L = 0$ is used only as a state-classification value, and δ is undefined.

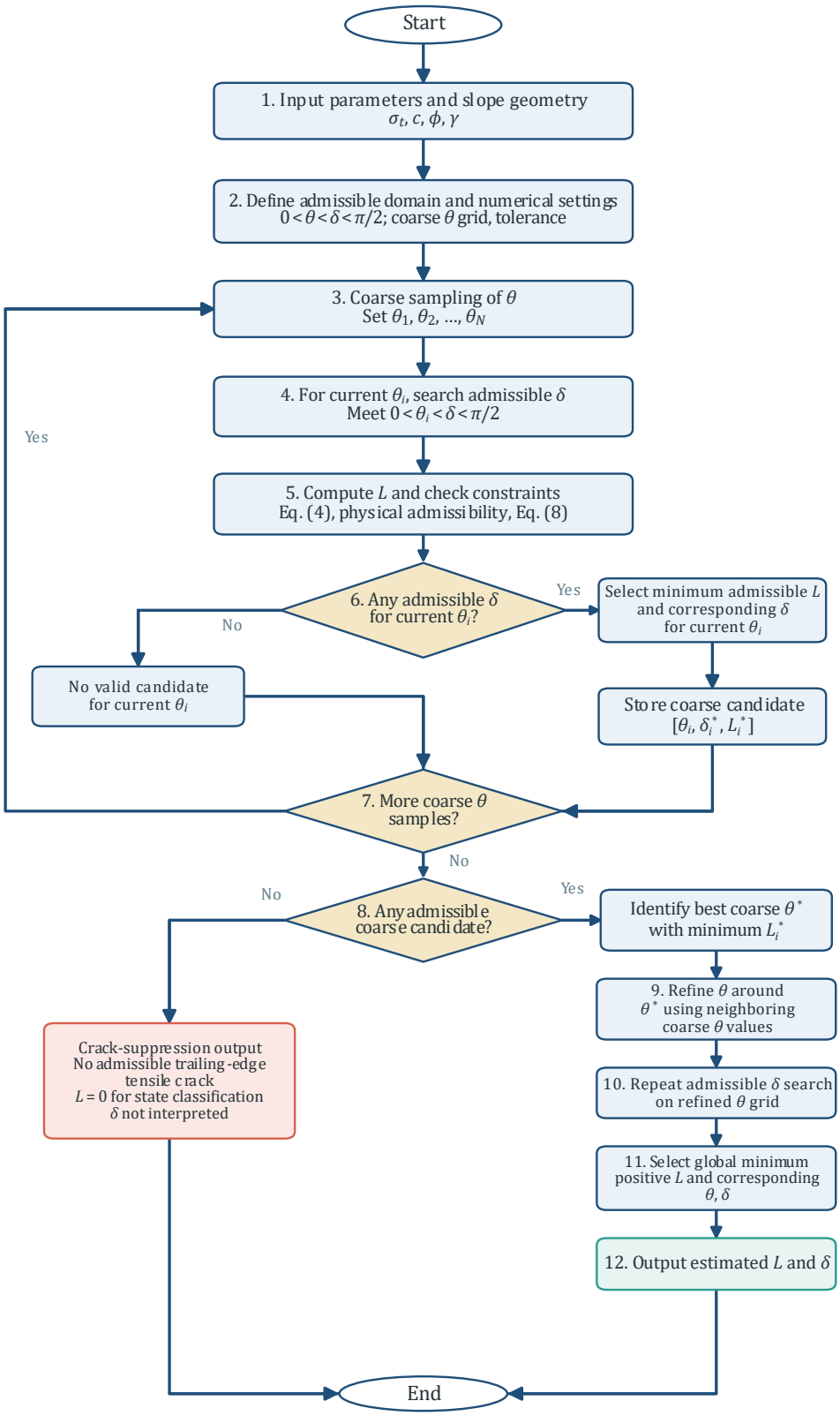


Fig. 5. Flowchart for admissible trailing-edge tensile-crack geometry search.

3. Comparisons with existing studies and MatDEM simulations

The formulation is examined through theoretical benchmarks, a bounded field

comparison, and DEM-extracted trailing-edge tensile cracks. The field and DEM cases involve observed or DEM-developed geometries, whereas the model returns an idealized local limit-state geometry. They are therefore treated as bounded consistency checks, not direct validation. Where tensile strength is not independently reported, $T = \sigma_t/c$ is used only as an auxiliary representation.

3.1 Theoretical benchmark comparisons

Existing theoretical solutions mainly focus on vertical trailing-edge tensile cracks; the corresponding crack-depth estimates are listed in Table 1 (Michalowski 2013; Spencer 1968; Zhang et al. 2018; Zhu et al. 2021).

Table 1. Vertical trailing-edge tensile-crack depth solutions.

Contributor(s)	Equation
Spencer	$L = \frac{2c}{\gamma}\sqrt{\frac{1+\sin\varphi}{1-\sin\varphi}}$
Michalowski	$L = \frac{3.83c}{\gamma}\tan\left(\frac{\pi}{4}+\frac{\varphi}{2}\right)$
Zhang et al.	$L = \frac{1+\sin\varphi-2\tan\theta\cos\varphi}{\cos^2\theta\times(1+\sin\varphi)(\tan\varphi-\tan\theta)}\frac{2c}{\gamma}$
Zhu et al.	$L = \frac{4c}{\gamma}\tan\left(\frac{\pi}{4}+\frac{\varphi}{2}\right)$

Table 1 defines c, γ and φ as cohesion, unit weight and friction angle, and θ as the potential shear-plane angle. Zhang et al. additionally require a prescribed φ and optimization with respect to θ. These benchmark equations are compared at the constitutive level of the Mohr–Coulomb parameters.

Fig. 6(a) compares the estimated theoretical crack depths under fixed soil properties (c = 20 kPa, γ = 18 kN/m^3, φ = 25°). The limit-state depth obtained from the present calculation decreases with increasing T, indicating that a higher tensile-strength ratio restricts the admissible penetration depth of the trailing-edge tensile crack. The compared solutions remain constant over the investigated T range because they do not treat tensile strength as an explicit variable, whereas the present model includes σ_t directly in the tensile-failure condition. Some approaches omit tensile strength, while others derive an equivalent value indirectly from c and φ. These different tensile-strength representations therefore produce different crack depth trends.

Fig. 6(b) illustrates the variation of crack depth with the internal friction angle φ under constant cohesion and unit weight, where T = 0.5 and T = 0.7 are considered for the present calculation. All models show an increasing trend of crack depth with increasing φ, and the present calculation gives broad benchmark consistency with existing theoretical solutions. For a given φ, the smaller T case gives a larger limit-state depth, which is consistent with the tensile strength dependency shown in Fig. 6(a). The comparison therefore indicates that the calculated limit-state depths remain within the range of established theoretical estimates

while introducing an explicit tensile strength.

Fig. 6(c) compares the influence of cohesion on limit-state depth for φ = 25°. The calculated depth increases with cohesion in all models, while the present calculation additionally distinguishes the two tensile strength ratios. Fig. 6 provides a theoretical benchmark showing that the limit-state calculation preserves the main parametric trends of existing solutions, and extends them by considering the effects of tensile strength.

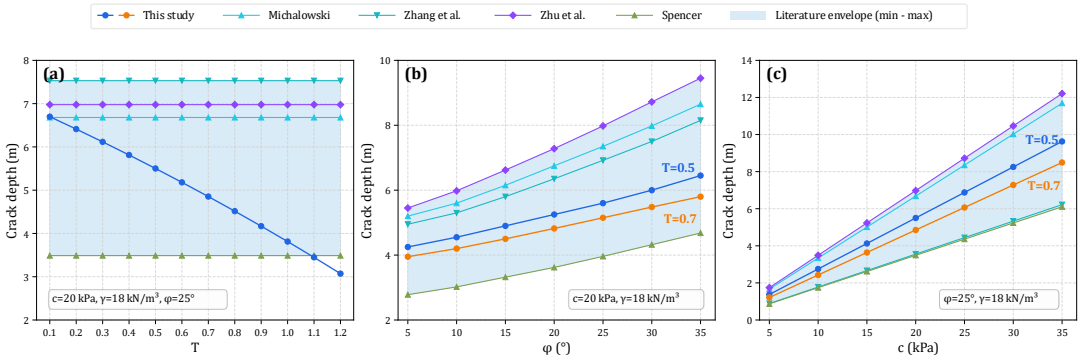


Fig. 6. Comparison between the present model and existing theoretical solutions: (a) case 1, (b) case 2 and (c) case 3.

3.2 Bounded comparison with a loess case

The field comparison uses the loess slope documented by Zhu et al. (2021) along the Huang-Yan Expressway in Fu County, Northwest China, where surveys reported a vertical trailing-edge tensile crack with an average depth of 12.78 m.

Table 2 lists the reported Mohr–Coulomb strength parameters obtained from unsaturated triaxial tests on samples collected within the crack zone (Zhu et al. 2021).

Table 2. Reported properties of undisturbed Malan loess.

Unit weight (kN/m³)	Unsaturated cohesion (kPa)	Internal friction angle (°)
17.59	51.3	36.1

The reported properties of undisturbed Malan loess are adopted directly from Zhu et al. (2021) without reinterpreting their physical origin. Thus, the case is used as a bounded comparison of the calculated crack depth response.

Fig. 7 shows that the calculated limit-state depth decreases from 21.80 m at T = 0.1 to 9.90 m at T = 1.0. The measured 12.78 m depth lies within this range and intersects the model curve between T = 0.7 and 0.8.

The tensile-strength ratio T was not independently constrained by a direct field σ_t measurement or a unique inversion of the observed crack depth in this comparison. For an illustrative tensile strength interval (σ_t = 5-30 kPa, corresponding approximately to T = 0.1-0.6 for c = 51.3 kPa), the calculated limit-state depths range from 15.61 m to 21.80 m. The field case therefore explores a bounded range of model responses rather than a calibrated site-specific reconstruction based on a unique tensile strength input.

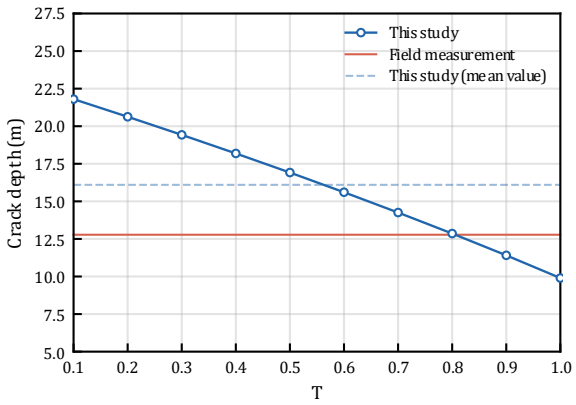


Fig. 7. Comparison of calculated limit-state depth with field-measured crack depth (Zhu et al. 2021).

3.3 Numerical consistency assessment with MatDEM simulations

3.3.1 DEM model configuration and simulation procedure

MatDEM was employed to provide DEM-assisted information for trailing-edge tensile-crack identification, including displacement, contact-force, bond-breakage and energy-related fields (Liu et al. 2013; Liu et al. 2017; Liu et al. 2021).

The numerical simulation followed a four-stage procedure as shown in Fig. 8, including initial particle generation, gravitational deposition, slope excavation and gravity-driven failure calculation.

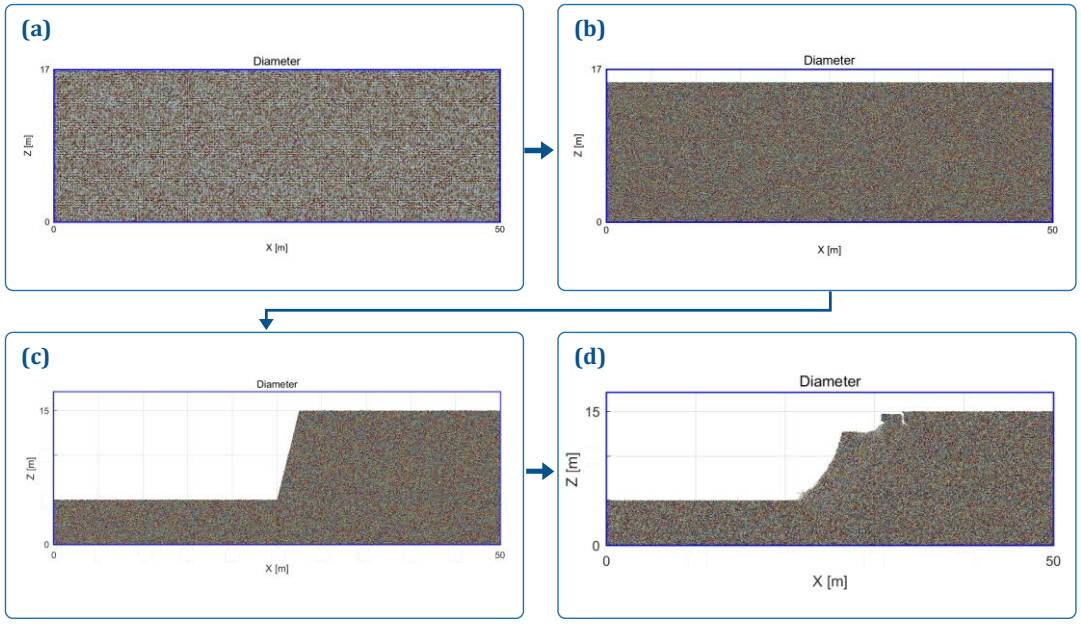


Fig. 8. Four-stage numerical simulation procedure: (a) model box construction, (b) gravity balance, (c) slope cut, and (d) gravity landslide.

Material parameters were assigned before gravitational deposition. The DEM calculation used a bonded linear elastic contact framework, and microscopic contact parameters were converted from target macroscopic parameters using the MatDEM conversion relationships of Liu et al. (2013, 2017, 2021). Other parameters used in the DEM simulations are listed in Table 3; detailed particle settings, boundary conditions, time integration parameters and output

controls are provided in the Appendix.

Here, H_e denotes the equivalent prototype slope height. Continuum σ_t is mapped to bonded-contact tensile strength, and different prototype heights are represented by scaling gravitational acceleration with $H_e/10$. The DEM simulations use the same target macroscopic strength parameters as the limit-state calculations.

Table 3. Parameters used in DEM simulations.

Case	c (kPa)	φ (°)	T	H_e (m)
1	7.38	14.77	0.79	7.45
2	25.31	50.62	0.99	29.65
3	4.19	8.38	0.60	3.31
4	26.29	52.58	1.47	27.75
5	14.48	28.96	0.67	14.13
6	16.19	32.39	0.58	18.10
7	6.42	12.84	1.26	7.94
8	9.32	18.64	1.34	7.95
9	5.84	11.67	0.82	6.49
10	13.33	26.67	0.69	16.06

3.3.2 Crack-parameter extraction from multi-physical field evolution

Trailing-edge tensile crack parameters were extracted from failed bonds and contact states using the workflow in Fig. 9. A representative step was selected after a connected trailing-edge tensile crack formed but before late-stage deformation distorted its trace. Candidate contacts were clustered by spatial continuity and topology; trailing-edge tensile clusters were retained, while toe, basal, isolated, and short secondary cracks were excluded. Detailed selection criteria and multi-field checks are given in the Appendix. If no dominant trailing-edge tensile cluster was identified, the case was classified as no crack.

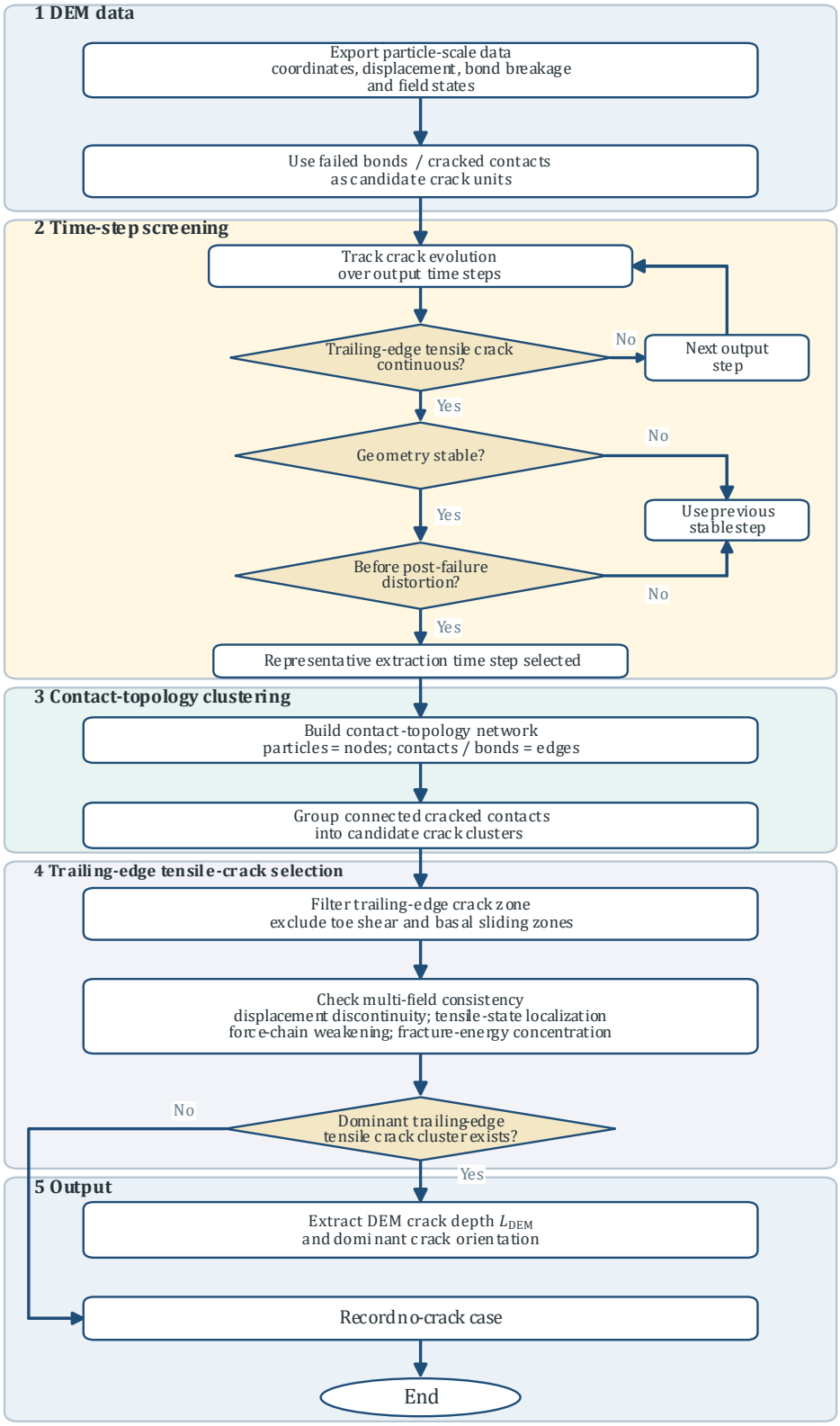


Fig. 9. Workflow for extracting a DEM-developed trailing-edge tensile crack.

As shown in Fig. 10, for the selected cluster, the DEM-extracted crack depth was measured from the slope-crest reference level to the deepest crack tip, and δ_{DEM} was obtained from the DEM-extracted dominant crack orientation. For a nearly straight crack, $\delta_{DEM} = \arctan|L_{DEM}/\Delta x|$;

for a curved or segmented cluster, the fitted centerline or principal direction was used.

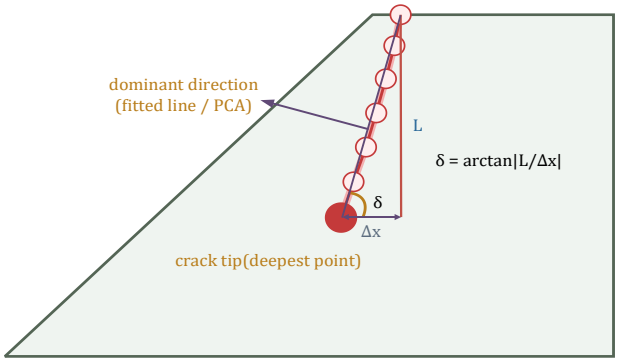


Fig. 10. Schematic definition of a DEM-developed trailing-edge tensile crack.

Case 10 was selected as a representative DEM simulation; Figs. A1–A3 in the Appendix illustrate deformation localization, trailing-edge tensile cracking, force-chain degradation and energy concentration, providing qualitative support for the selected failure stage.

3.3.3 Comparison between limit-state and DEM-extracted crack geometry

The DEM-extracted crack depth and inclination were obtained using the procedure in Sec. 3.3.2. The depth difference is defined as $|L_{limit} - L_{DEM}|$, whereas the angular difference is $\delta_{limit} - \delta_{DEM}$ and retains its sign. The depth relative difference is $|L_{limit} - L_{DEM}| / L_{limit} \times 100\%$, and the signed angular relative difference is $(\delta_{limit} - \delta_{DEM}) / \delta_{limit} \times 100\%$. The corresponding differences are summarized in Table 4. Case 4 corresponds to a high tensile-strength condition in which no identifiable trailing-edge tensile crack develops. Its analytical result is classified as a crack-suppression state, and it is excluded from the quantitative difference statistics of the nine cracked cases.

Table 4. Numerical consistency assessment between analytical limit-state geometry and DEM-extracted trailing-edge tensile-crack geometry.

Case	L_{limit} (m)	L_{DEM} (m)	δ_{limit} (°)	δ_{DEM} (°)	Depth difference (m)	Angular difference (°)	Depth relative difference (%)	Angular relative difference (%)
1	3.36	2.07	81.13	79.59	1.29	1.54	38.39	1.90
2	2.96	0.57	76.41	84.79	2.39	-8.38	80.74	-10.97
3	4.47	2.63	83.11	85.10	1.84	-1.99	41.16	-2.39
4	No crack	No crack	—	—	—	—	n/a	n/a
5	4.02	1.82	81.70	85.00	2.20	-3.30	54.73	-4.03
6	3.76	1.85	82.61	76.93	1.91	5.68	50.80	6.88
7	2.09	1.16	77.47	90.00	0.93	-12.53	44.50	-16.17
8	2.89	0.80	76.32	77.98	2.09	-1.66	72.32	-2.18
9	2.95	2.01	81.02	83.05	0.94	-2.03	31.86	-2.51
10	3.18	1.86	81.57	80.72	1.32	0.85	41.51	1.04

Fig. 11 compares the calculated limit-state and DEM-extracted crack geometries and their relative differences. For depth, the calculated limit-state values range from 2.09 m to 4.47 m for the nine cracked cases, whereas the DEM-extracted values range from 0.57 m to 2.63 m. As shown in Table 4 and Fig. 11(a), the limit-state calculation generally gives larger depths than those extracted from the DEM simulations. Excluding the crack-suppression Case 4, the MAE and RMSE of depth are 1.66 m and 1.74 m, respectively, and the mean relative difference is 50.67%, as shown in Fig. 11(c). This difference should be interpreted in terms of definition: calculated L is a limit-state reference depth, whereas the DEM-extracted value is the developed crack depth identified during the numerical failure process.

For the limit-state inclination δ, the calculated values range from 76.32° to 83.11° for the nine cracked cases, while the DEM-extracted values range from 76.93° to 90.00°. As shown in Fig. 11(b), most data points are distributed near the 1:1 line, indicating that the calculated inclination angle is broadly consistent with the DEM-extracted dominant crack orientation. Excluding Case 4, the MAE and RMSE of the inclination angle are 4.22° and 5.62°, respectively, and the mean absolute relative difference is 5.34%, as shown in Figs. 11(b) and (d). Within this DEM-based comparison, δ appears less affected by crack-tip identification than L and therefore provides a more stable descriptor of the DEM-extracted dominant crack orientation.

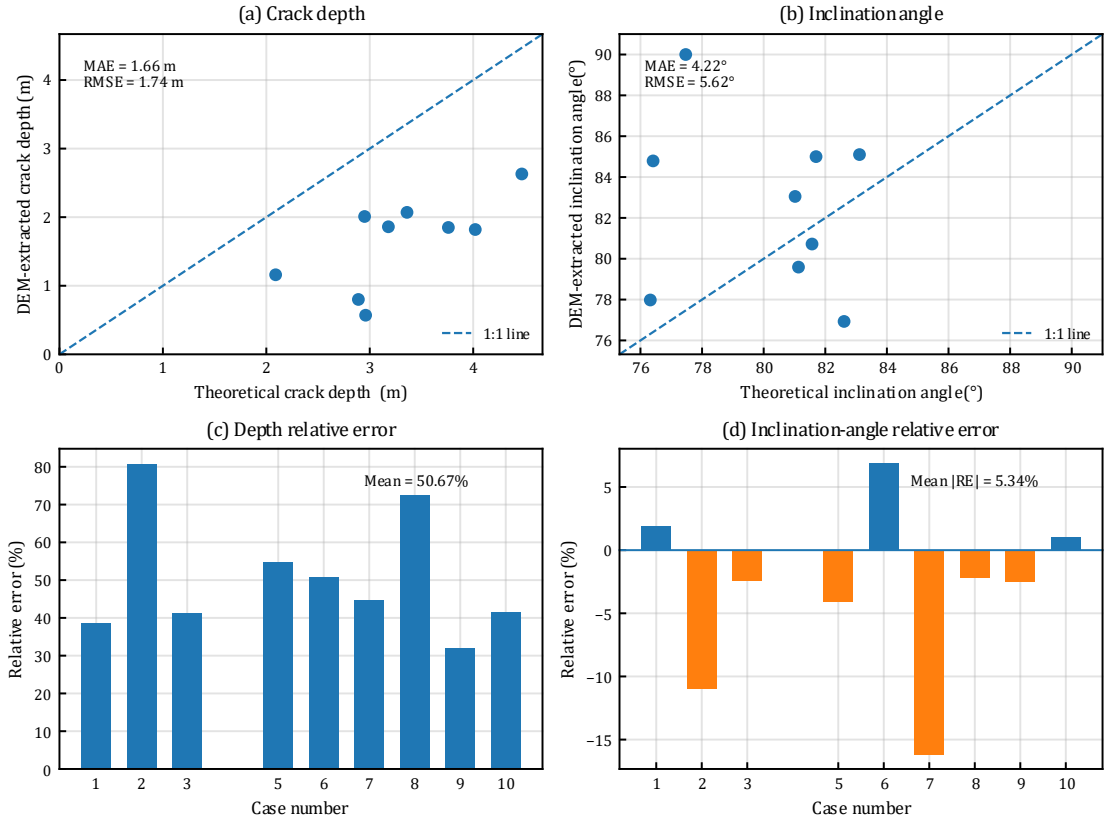


Fig. 11. Comparison of analytical limit-state and DEM-extracted crack geometry: (a) depth, (b) analytical inclination and DEM-extracted dominant crack orientation, (c) depth relative difference, and (d) signed angular relative difference.

Particle discreteness, packing variability and local bond failure introduce variation in

DEM crack development, while particle size limits crack-tip identification, particularly for shallow cracks. The idealized limit-state geometry differs from curved, segmented and locally discontinuous DEM traces. Extracted depth also depends on the identification stage because late-stage deformation and particle rearrangement may obscure the earlier crack trace.

Overall, the DEM comparison preserves the crack/no-crack distinction and shows closer correspondence for the dominant crack orientation than for depth.

4. Effects of soil parameters on limit-state crack geometry

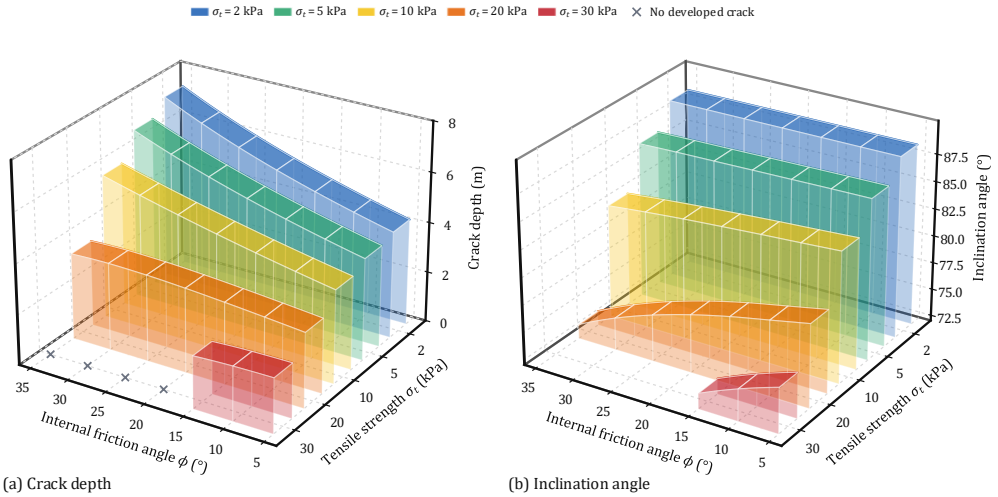
4.1 Parametric effects on limit-state depth and inclination of crack

Four parameters are varied independently: tensile strength σ_t, cohesion c, internal friction angle φ and unit weight γ. The adopted ranges are σ_t = 2–30 kPa, c = 5–35 kPa, φ = 5°–35° and γ = 18–24 kN/m^3. Unless otherwise stated, the baseline values are σ_t = 10 kPa, c = 20 kPa, φ = 25° and γ = 20 kN/m^3. These ranges define the response domain of the model and should not be interpreted as covering all soil conditions. The one-at-a-time scans isolate model-internal effects; they do not represent the coupled evolution of strength parameters under a changing material or hydro-mechanical state. Suppression cases L are retained in the depth plots, whereas δ is omitted because it is undefined for these cases

4.1.1 Effect of tensile strength

Fig. 12 shows the responses of limit-state depth L and trailing-edge tensile crack inclination δ to tensile strength σ_t at fixed c = 20 kPa and γ = 20 kN/m^3, with φ as the grouping parameter. In all finite positive depth cases, increasing σ_t reduces L. For φ = 25°, L decreases from 6.03 m at σ_t = 2 kPa to 4.95 m at 10 kPa, and the solution enters crack suppression at 30 kPa. The separation among the L curves also decreases as σ_t increases, indicating that the influence of φ becomes less pronounced as the tensile strength becomes more restrictive. This occurs because an increasing tensile threshold progressively restricts the range of trailing-edge tensile crack geometries, reducing the relative influence of shear-strength-related parameters. Groups with larger φ terminate earlier, showing that the suppression boundary depends on both tensile and shear strengths.

Within each finite positive depth branch, δ also decreases with increasing σ_t. At φ = 25°, it decreases from 88.58° at σ_t = 2 kPa to 83.08° at 10 kPa. The reduction is gradual at low φ but steeper at larger φ, where the branch terminates earlier. Therefore, increasing σ_t not only reduces the limit-state depth but also contracts the corresponding trailing-edge tensile crack inclination range before the finite positive depth state transitions to suppression.



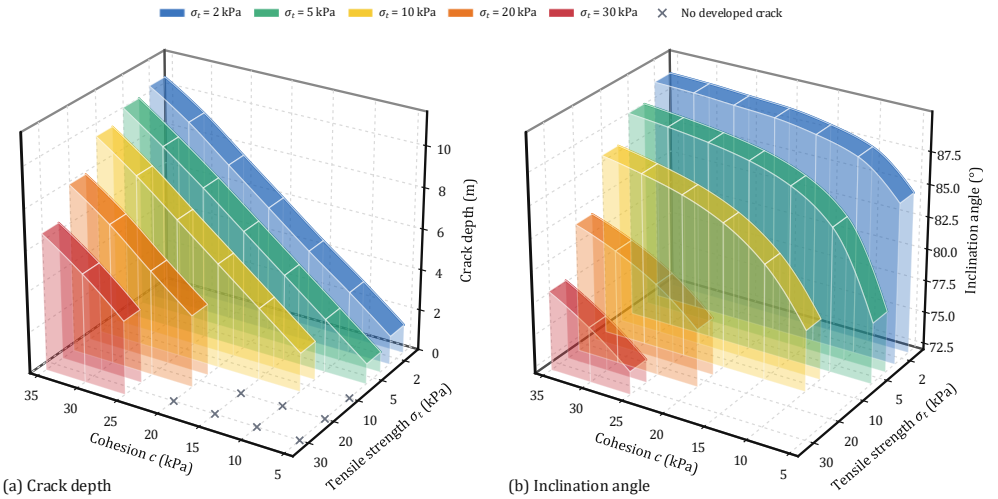
(a) Crack depth (b) Inclination angle

Fig. 12. Effect of tensile strength σ_t on limit-state depth and inclination under different internal friction angles: (a) limit-state depth and (b) trailing-edge tensile-crack inclination.

4.1.2 Effect of cohesion

Fig. 13 shows the responses of limit-state depth L and trailing-edge tensile crack inclination δ to cohesion c at fixed $\varphi = 25°$ and $\gamma = 20$ kN/m^3, with σ_t as the grouping parameter. Increasing c generally expands the range of conditions producing a finite positive depth solution and increases L once a finite positive depth state is reached. At σ_t = 10 kPa, the response changes from crack suppression at c = 5 kPa to L = 4.95 m at c = 20 kPa and 9.70 m at c = 35 kPa. At σ_t = 30 kPa, suppression persists at c = 5–20 kPa, whereas L increases from 3.46 m at c = 25 kPa to 6.80 m at 35 kPa. Cohesion therefore affects both the magnitude of L and the occurrence of a finite-positive-depth solution.

Within the finite positive depth regime, δ increases with c, but the increment progressively diminishes toward a plateau. The absolute inclination decreases as σ_t increases, and under high tensile strength δ appears only after c becomes sufficient to permit a finite positive depth solution. Cohesion therefore affects both the finite positive depth solution regime and the limit-state depth.



(a) Crack depth (b) Inclination angle

Fig. 13. Effect of cohesion on limit-state depth and inclination under different tensile strengths: (a) limit-

state depth and (b) trailing-edge tensile-crack inclination.

4.1.3 Effect of internal friction angle

Fig. 14 shows the responses of limit-state depth L and trailing-edge tensile crack inclination δ to internal friction angle φ at fixed c = 20 kPa and γ = 20 kN/m^3, with σ_t as the grouping parameter. The effect of φ depends strongly on tensile strength. At low-to-moderate σ_t, increasing φ increases L. For σ_t = 10 kPa, L rises from 3.71 m at φ = 5° to 4.95 m at 25° and 5.71 m at 35°, an increase of approximately 54%. Similar monotonic increases occur at σ_t = 2 and 5 kPa. At higher σ_t, however, the response weakens: at 20 kPa the increase progressively flattens and slightly reverses at large φ, while at 30 kPa only the lower-φ combinations retain finite positive depth solutions. The effect of φ on L is therefore not universally monotonic. This non-monotonic behavior results from the competition between increased shear resistance and the restrictive effect of the tensile-strength threshold. Increasing φ enhances the shear resistance component, but under high tensile strength the trailing-edge tensile crack geometry is primarily limited by the tensile condition rather than the shear condition.

The angular response is likewise conditional on σ_t. At low tensile strength, δ changes little with φ; at σ_t = 10 kPa, it decreases from 84.03° at φ = 5° to 82.42° at 35°, and at higher σ_t the decrease becomes more pronounced before the finite positive depth branch terminates. Thus, the influence of friction angle on the trailing-edge tensile crack geometry cannot be interpreted independently of tensile strength because both parameters jointly affect the resulting tensile–shear equilibrium state.

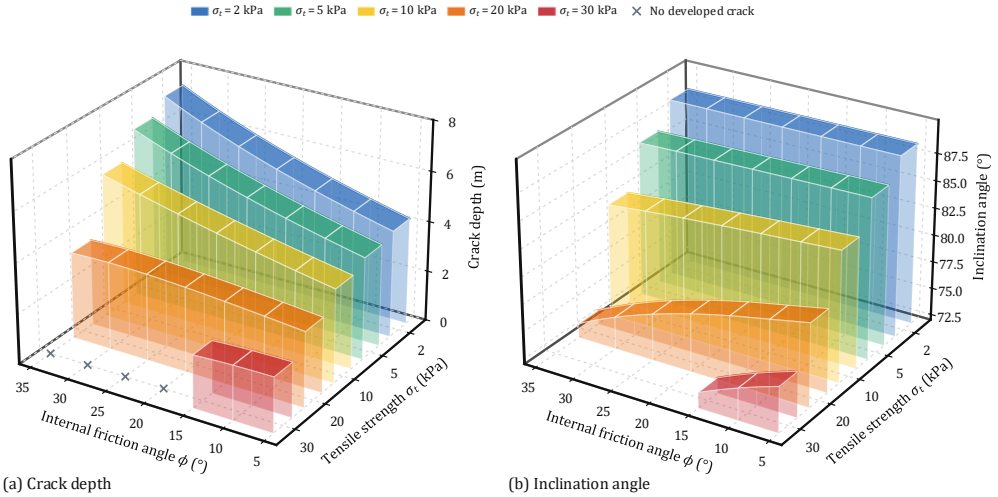


Fig. 14. Effect of internal friction angle on limit-state depth and inclination under different tensile strengths: (a) limit-state depth and (b) trailing-edge tensile-crack inclination.

4.1.4 Effect of unit weight

Fig. 15 shows the responses of limit-state depth L and trailing-edge tensile-crack inclination δ to unit weight γ at fixed c = 20 kPa and φ = 25°, with σ_t as the grouping parameter. For all finite-positive-depth groups, increasing γ monotonically reduces L, and the depth curves remain approximately parallel. At σ_t = 10 kPa, L decreases from 5.50 m at γ = 18 kN/m^3

to 4.95 m at 20 kN/m^3 and 4.13 m at 24 kN/m^3, corresponding to a reduction of approximately 25%. Similar reductions occur in the other finite positive depth groups, whereas the σ_t = 30 kPa condition remains in crack suppression throughout the investigated range.

Within each fixed-σ_t finite positive depth branch, δ remains essentially constant with γ, producing nearly horizontal curves in Fig. 15(b). This indicates that unit weight primarily changes the gravitational stress contribution and the limit-state depth, with limited influence on the selected trailing-edge tensile crack inclination under fixed strength conditions. The absolute inclination differs among tensile strength groups, but the isolated unit-weight effect is primarily a depth shift rather than a rotation of the selected trailing-edge tensile crack.

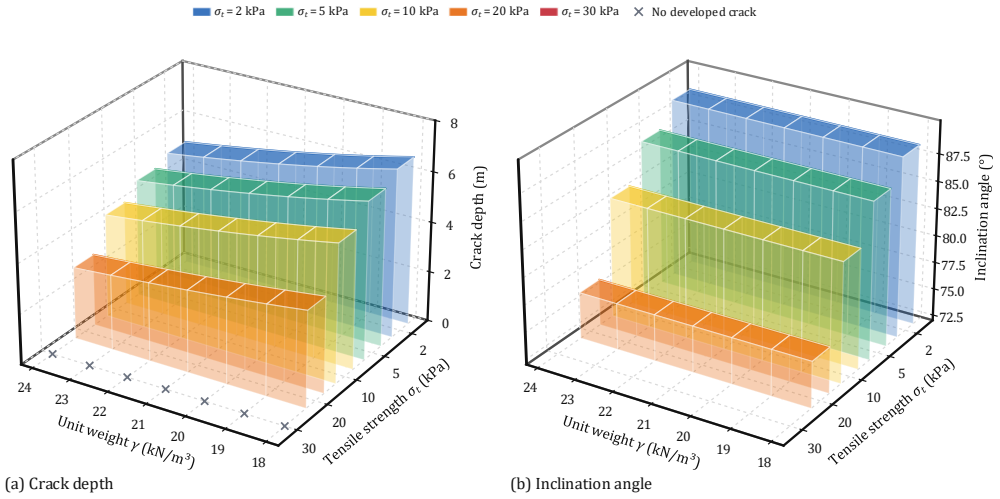


Fig. 15. Effect of unit weight on limit-state depth and inclination under different tensile strengths: (a) limit-state depth and (b) trailing-edge tensile-crack inclination.

4.2 Sensitivity and interaction effects of soil parameters

4.2.1 Local sensitivity under the baseline condition

Table 5 reports a one-at-a-time local sensitivity analysis under the baseline condition σ_t = 10 kPa, c = 20 kPa, φ = 25°, and γ = 20 kN/m^3. In this analysis, only one input parameter is perturbed by +10% while the remaining parameters are held constant, so the table describes near-baseline response slopes rather than an importance ranking over the full parameter space. The relative sensitivity coefficient is defined as (Campolongo et al. 2000; Saltelli 2002; Saltelli et al. 2006):

$$S = \frac{(Y - Y_0) / Y_0}{(P - P_0) / P_0} \tag{15}$$

where Y represents the response variable, namely limit-state depth L or trailing-edge tensile-crack inclination δ; P represents the input parameter, namely σ_t, c, φ, or γ; and the subscript 0 denotes the baseline value.

For the limit-state depth L, the absolute local sensitivity ranking is c (S_L = +1.2855) > γ (S_L = -0.9091) > φ (S_L = +0.3640) > σ_t (S_L = -0.2891). The sensitivity signs are consistent with the mechanical mechanism of the proposed framework: increasing tensile strength raises the tensile failure threshold and reduces the limit-state depth, whereas increasing cohesion and

friction angle enhances the shear-resistance component and increases the limit-state depth near the baseline condition. Increasing unit weight increases the gravitational stress contribution and reduces L. For trailing-edge tensile crack inclination, the local coefficients are smaller, with S_δ = -0.0819 for σ_t, +0.0723 for c, -0.0184 for φ, and approximately 0 for γ. This indicates that the trailing-edge tensile-crack inclination is less sensitive to small perturbations around the baseline condition than the limit-state depth.

Table 5. Local sensitivity coefficients under the baseline condition.

Parameter	P_0	$\Delta P/P_0$	S_L	S_δ
σ_t	10 kPa	0.10	-0.2891	-0.0819
c	20 kPa	0.10	+1.2855	+0.0723
φ	25°	0.10	+0.3640	-0.0184
γ	20 kN/m^3	0.10	-0.9091	+0.0000

4.2.2 Global sensitivity and interaction effects

To quantify variance contributions when all input parameters vary simultaneously, Sobol global sensitivity analysis was performed. The four input variables were treated as independent uniform variables, with σ_t = 2 to 30 kPa, c = 5 to 35 kPa, φ = 5° to 35°, and γ = 18 to 24 kN/m^3. Saltelli/Sobol sampling was performed with a final base sample size of N = 4096. For four input parameters and second-order Sobol analysis, this produced 40960 model evaluations.

For this analysis, the response was defined as a zero-including limit-state depth/suppression response, denoted as L^*. For samples with an admissible finite positive depth geometry, L^* is equal to the calculated limit-state depth L. For samples without an admissible finite positive depth geometry, the response was assigned L^* = 0 and the sample was classified as a crack-suppression state. Under the prescribed input distributions, 37976 samples produced finite positive depth geometries, whereas 2984 samples were classified as crack-suppression cases, corresponding to 7.29% of all model evaluations.

In the Sobol framework, S_1 denotes the first-order Sobol sensitivity index, which measures the direct contribution of an individual parameter to the output variance. S_T denotes the total-order Sobol sensitivity index, which includes both the direct contribution and all interaction effects involving that parameter. The difference S_T - S_1 is therefore used here as an interaction index, indicating the degree to which a parameter participates in coupled effects with other parameters. The two indices are calculated as (Saltelli et al. 2010):

$$\begin{cases} S_{1,i} = \dfrac{Var_{X_i}(E_{X_{\sim i}}(Y \mid X_i))}{Var(Y)} \\ S_{T,i} = \dfrac{E_{X_{\sim i}}(Var_{X_i}(Y \mid X_{\sim i}))}{Var(Y)} \end{cases} \tag{16}$$

where Y denotes the model output, either L^* or the diagnostic inclination-angle response;

X_i denotes the i-th input parameter; and $X_{\sim i}$ denotes all input parameters except X_i.

Table 6 summarizes the first-order index S_1, the total-order index S_T, and the interaction index S_T - S_1 for L^* and for the diagnostic angular response. For L^*, cohesion has the largest total-order contribution to the variance of the zero-including limit-state depth/suppression response, with S_1 = 0.7678 and S_T = 0.8201. Tensile strength σ_t ranks second by S_T, with S_1 = 0.1371 and S_T = 0.1895, followed by φ and γ.

The inclination angle response was also analyzed using the same sample treatment, but its indices should be regarded as diagnostic only. Because δ is not physically defined for crack-suppression samples, the assigned zero values in those samples act only as numerical placeholders. Therefore, these angular indices describe the statistical behavior of the adopted sampling treatment rather than the intrinsic sensitivity of trailing-edge tensile crack inclination when an admissible finite-positive-depth trailing-edge tensile crack exists.

Under this diagnostic definition, c, σ_t and φ show large interaction indices of 0.4430, 0.3855 and 0.3587, respectively, whereas γ has no meaningful contribution in the reported angular response.

The difference between local and global sensitivity rankings results from their different definitions. Local sensitivity describes parameter effects near a specific baseline state, whereas Sobol indices quantify variance contributions over the full parameter domain and include nonlinear interactions and state transitions. Therefore, the two rankings are not contradictory. For L^*, cohesion remains the dominant parameter in both analyses, while tensile strength becomes more influential in the global analysis because it affects both continuous depth variation and the transition between finite-positive-depth and crack-suppression states. All sensitivity results are conditional on the adopted model formulation, parameter ranges, and output definitions.

Table 6. Global Sobol sensitivity indices for the zero-including limit-state-depth/suppression response L^* and diagnostic inclination-angle response under the prescribed input distributions.

Response	Parameter	S_1	S_T	S_T - S_1	Rank by S_T
L^* zero-including crack-depth/suppression response	c	0.7678	0.8201	0.0522	1
	σ_t	0.1371	0.1895	0.0524	2
	φ	0.0098	0.0588	0.0490	3
	γ	0.0113	0.0184	0.0071	4
δ diagnostic angular response	c	0.3019	0.7449	0.4430	1
	σ_t	0.1504	0.5358	0.3855	2
	φ	0.0638	0.4225	0.3587	3

Response	Parameter	S_1	S_T	S_T - S_1	Rank by S_T
	γ	0.0000	0.0000	0.0000	4

5. Model interpretation, applicability and limitations

5.1 Interpretation of model states, strength parameters, and model scope

The finite positive depth and crack-suppression states are defined in Sec. 2.4. The corresponding L and δ describe a local limit-state geometry rather than the time-dependent geometry of a propagating field crack.

The resulting geometry may be used as a mechanically constrained reference for failure interpretation, back-analysis, or subsequent analyses. It does not represent the developed crack depth during a complete slope-failure process, which additionally depends on global slope geometry, loading conditions, and progressive deformation.

The present formulation is restricted to cemented soils under drained conditions whose macroscopic shear response can be reasonably represented by the Mohr–Coulomb criterion and that exhibit finite tensile resistance. Here, c and φ denote the drained Mohr–Coulomb cohesion intercept and friction angle, respectively, while tensile failure is governed independently by the macroscopic tensile strength σ_t. These strength parameters are assumed to characterize the same prescribed material state.

For cemented soils, interparticle bonding can permit a non-zero shear strength intercept to persist under drained shearing and can also provide finite tensile resistance. The present formulation does not explicitly model the micromechanical origin, evolution, or degradation of cementation; instead, c, φ, and σ_t are treated as macroscopic strength parameters characterizing the prescribed drained state.

Saturated fine-grained soils under undrained loading are commonly characterized by the undrained shear strength s_u in a total-stress analysis. Such undrained conditions are outside the scope of the present formulation. The model does not simulate drainage or pore-pressure evolution; the prescribed strength parameters represent the drained material condition used in the limit-state calculation.

5.2 Applicability and limitations

The formulation represents an idealized two-dimensional homogeneous cemented soil slope with an initially intact tensile-shear failure mechanism. It is therefore most applicable when the local failure process can be reasonably represented by a trailing-edge tensile crack and a lower shear surface. The trailing-edge tensile crack is straight, and the lower boundary is represented by an idealized shear plane. Geological heterogeneity, stratification, pre-existing fissures, and spatially variable strength distributions may alter local stress redistribution and failure paths; therefore, additional geological characterization or more advanced numerical approaches are required for such conditions.

Three-dimensional topography and out-of-plane deformation may introduce additional

stress redistribution and spatial crack morphology that cannot be fully represented by the present two-dimensional framework.

The EF normal pressure is approximated as linear, with its resultant at one-third of the corresponding height. This assumption provides a tractable representation for moment equilibrium but may differ from the actual nonlinear stress distribution along the shear boundary. Consequently, the calculated L and δ should be interpreted within the adopted limit-state framework.

The fixed-parameter formulation does not represent transient pore-pressure changes, hydraulic-state-dependent strength evolution, progressive degradation of cementation, or progressive cracking such as propagation, branching and coalescence. Such time-dependent hydro-mechanical and fracture processes require coupled seepage–mechanical or fracture-based formulations beyond the current limit-state approach.

6. Conclusions

This study develops a limit-state framework for trailing-edge tensile-crack geometry in cemented soil slopes under drained conditions. Rather than prescribing crack inclination as a geometric input, the framework treats limit-state crack depth and inclination as coupled unknowns constrained simultaneously by tensile failure, shear failure, equilibrium, and geometric admissibility. Tensile strength is explicitly introduced as the tensile-failure threshold. The framework is examined using theoretical benchmarks, a bounded field comparison, controlled DEM simulations, and parametric and sensitivity analyses. The main conclusions are:

1. Theoretical benchmarks reproduce established crack-depth trends, the loess field depth lies within the calculated limit-state range for the adopted T interval, and the DEM comparison preserves the crack/no-crack distinction with closer correspondence for inclination than for depth. Accordingly, L is interpreted as a local limit-state reference, while δ shows bounded correspondence with the DEM-extracted dominant crack orientation.
2. Increasing tensile strength reduces L and δ and can suppress the positive depth solution; increasing cohesion generally increases both within finite positive depth cases; increasing unit weight reduces L with little effect on δ; and the effect of friction angle depends strongly on tensile strength, becoming weakly non-monotonic as the suppression boundary is approached.
3. Local sensitivity identifies cohesion and unit weight as the strongest near-baseline controls on L, whereas the global Sobol analysis ranks cohesion > tensile strength > friction angle > unit weight for the combined limit-state-depth/suppression response L^*. Cohesion dominates the variance over the adopted domain, while tensile strength remains important through its influence on the transition between finite-positive-depth and crack-suppression states. These rankings are conditional on the adopted parameter

ranges and output definitions.

Appendix

The DEM calculation used a 50 m × 17 m rectangular domain under a two-dimensional plane-strain idealization. The soil mass was discretized into 23,286 spherical particles with an average diameter of 0.04 m and a uniformity coefficient of 0.5. The calculation consisted of initial particle generation, gravitational deposition, slope excavation, and gravity-driven failure calculation. Material assignment used density ρ = 2000 kg/m^3, Poisson's ratio ν = 0.2, elastic modulus E = 5.0 MPa, and a bonded linear elastic contact framework. Contact parameters were converted from the target macroscopic parameters using the MatDEM conversion relationships. The explicit time step was 4×10^{-4} s, and each case was run for 20,000 steps. Fixed walls were used at the base and lateral sides, and the top boundary was free. Different equivalent prototype heights H_e were represented by scaling gravitational acceleration by $H_e/10$.

For the DEM reference cases, T is used only as an auxiliary tensile-strength ratio for defining the DEM cases. The representative extraction time step was selected when the trailing-edge tensile crack became continuous and its geometry was relatively stable before strong post-failure distortion. Failed bonds and cracked contacts were used as candidate crack units. Candidate clusters were grouped according to spatial continuity and contact topology. Clusters in the trailing-edge region were retained, whereas cracks associated with the toe shear zone, basal sliding zone, isolated local bond breakage, or short secondary cracks were excluded.

The dominant trailing-edge tensile crack was defined as the connected cluster that was spatially continuous near the trailing edge of the slope and mechanically consistent with the tensile-dominated failure zone. The crack tip was taken as the deepest point of this cluster. The DEM-extracted crack depth was measured as the vertical projection from the slope-crest reference level to the deepest crack tip. For a nearly straight trailing-edge tensile crack, the DEM-extracted inclination was obtained from the endpoint relation. For a curved or segmented cluster, the dominant crack orientation was estimated from the fitted centerline or principal direction of the cluster coordinates. If no dominant trailing-edge tensile-crack cluster was identified at the representative extraction time step, the case was recorded as no crack.

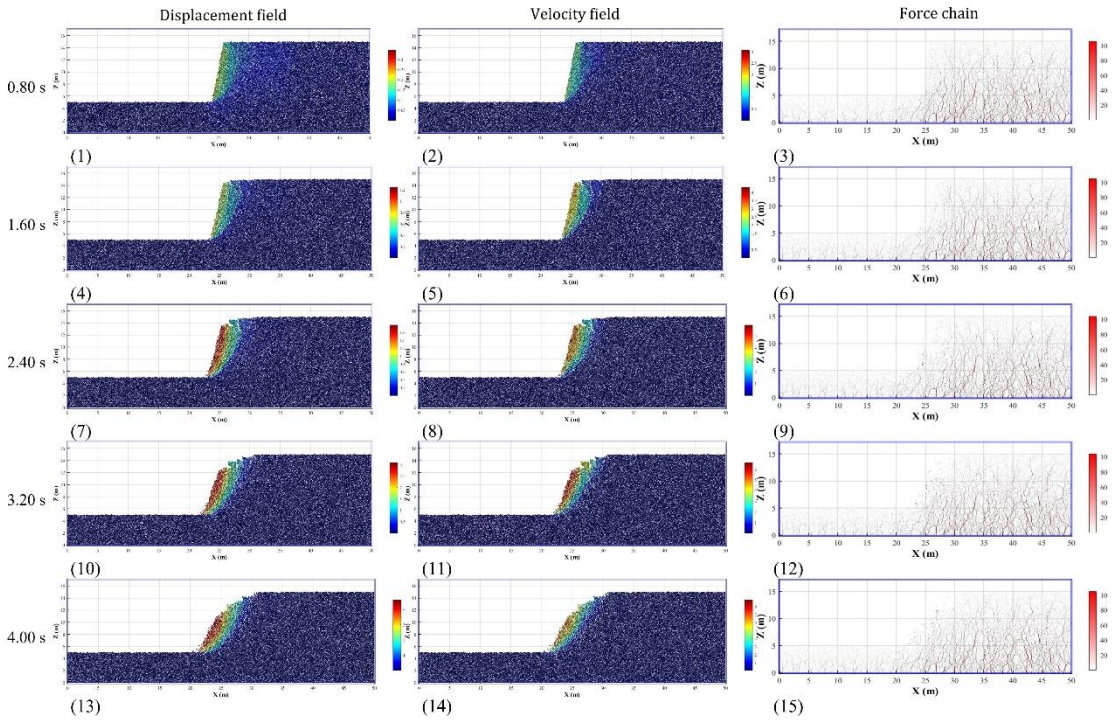


Fig. A1. Evolution of displacement, velocity and force chain.

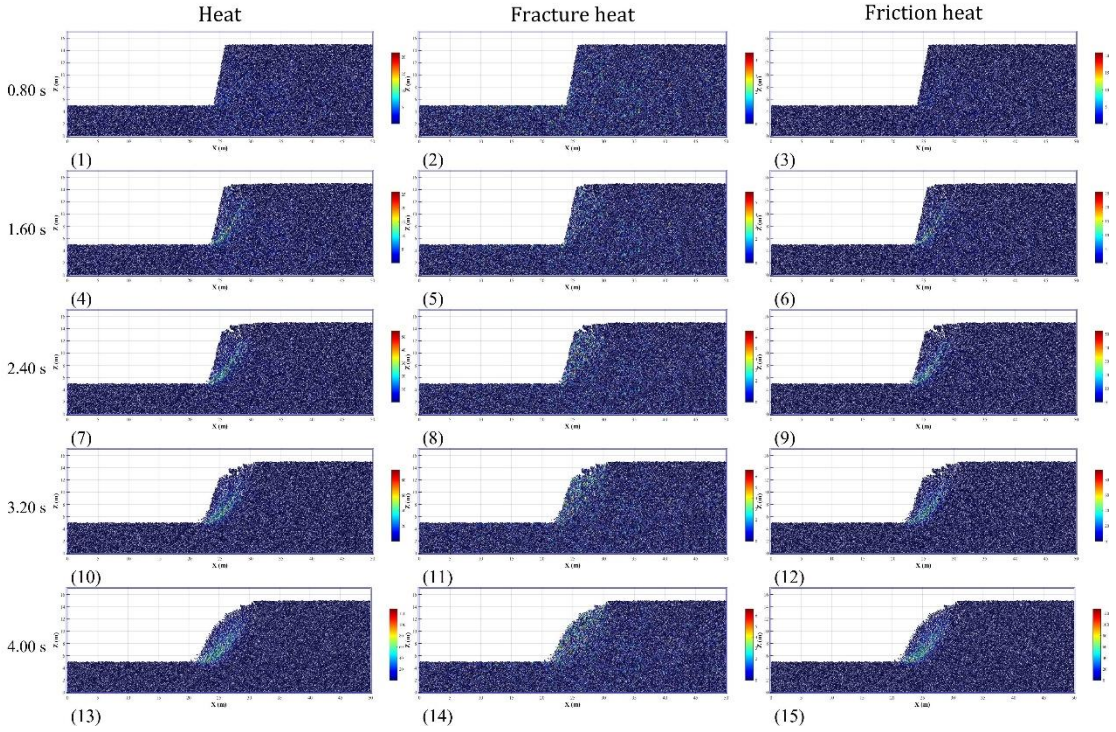


Fig. A2. Evolution of heat, fracture heat and friction heat.

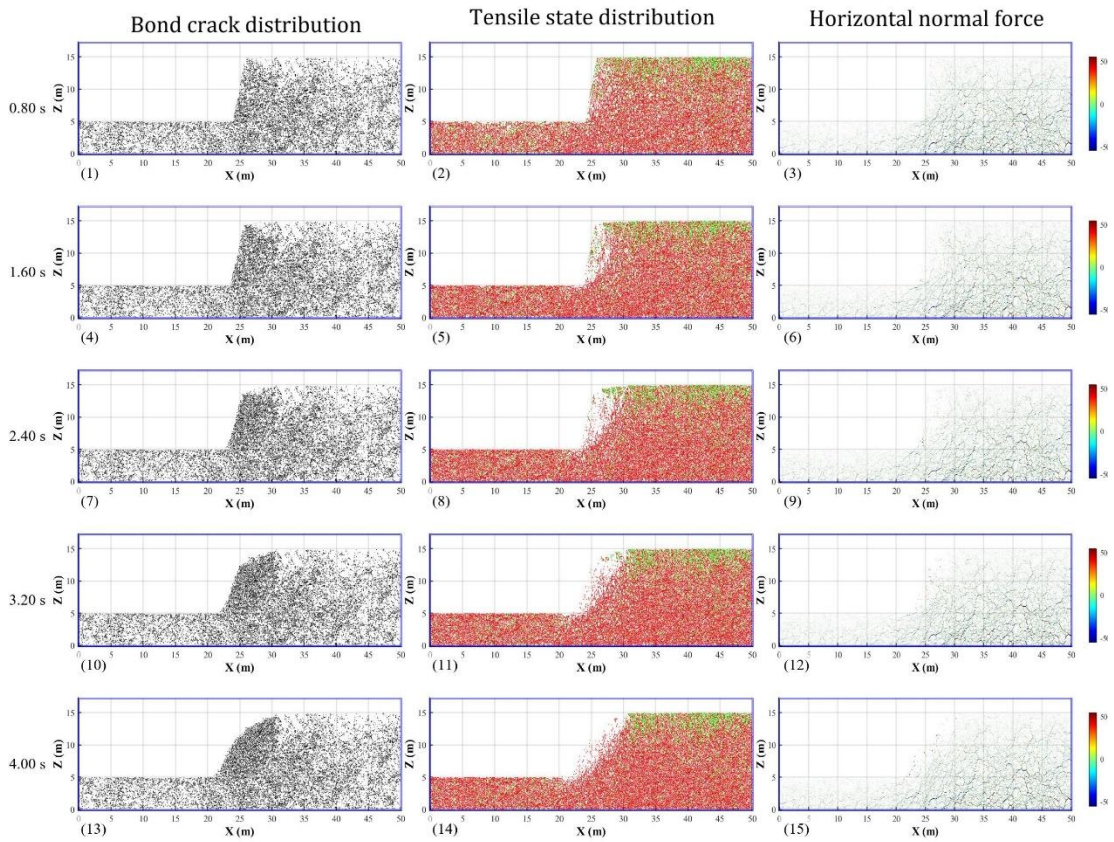


Fig. A3. Evolution of bond crack, tensile state and horizontal normal force.

References

Bao, Y., Li, Y., Zhang, Y., Yan, J., Zhou, X., Zhang, X., 2022. Investigation of the role of crown crack in cohesive soil slope and its effect on slope stability based on the extended finite element method. Natural Hazards 110, 295–314. https://doi.org/10.1007/s11069-021-04947-8

Bulolo, S., Leong, E.C., Kizza, R., 2021. Tensile strength of unsaturated coarse and fine-grained soils. Bulletin of Engineering Geology and the Environment. https://doi.org/10.1007/s10064-020-02073-6

Campolongo, F., Saltelli, A., Tarantola, S., 2000. Sensitivity anaysis as an ingredient of modeling. Statistical Science 15, 377–395. https://doi.org/10.1214/ss/1009213004

Chen, X., Jing, X., Li, X., Chen, J., Ma, Q., Liu, X., 2023. Slope Crack Propagation Law and Numerical Simulation of Expansive Soil under Wetting–Drying Cycles. Sustainability 15, 5655. https://doi.org/10.3390/su15075655

Chen, X., Tang, C., Luo, Y., Vahedifard, F., Tian, B., Wang, T., Zeng, Z.-J., Cheng, Q., 2025. Exploring the hysteresis effects of climate-induced desiccation cracks on slope stability: New insights from experimental and numerical studies. Journal of Geophysical Research: Earth Surface 130, e2024JF008085. https://doi.org/10.1029/2024jf008085

Deng, L., Yuan, H., Chen, J., Sun, Z., Fu, M., Zhou, Y., Yan, S., Zhang, Z., Chen, T., 2019. Experimental investigation on progressive deformation of soil slope using acoustic emission monitoring. Engineering Geology 261, 105295. https://doi.org/10.1016/j.enggeo.2019.105295

Dwiantara, M.S., Faris, F., Fathani, T.F., 2023. Effect of tension crack on slope stability in rainfall conditions. AIP Conference Proceedings 2791, 030004. https://doi.org/10.1063/5.0130107

Fang, K., Fu, Y., Tang, H., Gao, T., An, P., Wu, Q., 2025. Landslide model tests with a miniature 2D principal stress

sensor. Journal of Rock Mechanics and Geotechnical Engineering 17, 94–105. https://doi.org/10.1016/j.jrmge.2023.12.025

Gao, Y., Song, W., Zhang, F., Qin, H., 2015. Limit analysis of slopes with cracks: Comparisons of results. Engineering Geology 188, 97–100. https://doi.org/10.1016/j.enggeo.2015.01.013

He, Y., Yu, J., Yuan, R., Wang, W., Nikitas, N., 2022. Stability and failure mechanisms in three-dimensional cracked slope: Static and dynamic analysis. Computers and Geotechnics 144, 104626. https://doi.org/10.1016/j.compgeo.2021.104626

Hu, C., Zeng, Y.-h., Yao, H., 2024. Stability analysis of slopes with cracks using the finite element limit analysis method. Frontiers in Earth Science 12.

Jia, J., Mao, C., Tenorio, V.O., 2024. Slope stability considering multi-fissure seepage under rainfall conditions. Scientific Reports 14, 11662. https://doi.org/10.1038/s41598-024-62387-3

Liu, C., Liu, H., Zhang, H., 2021. MatDEM-fast matrix computing of the discrete element method. Earthquake Research Advances 1, 100010. https://doi.org/10.1016/j.eqrea.2021.100010

Liu, C., Pollard, D.D., Shi, B., 2013. Analytical solutions and numerical tests of elastic and failure behaviors of close-packed lattice for brittle rocks and crystals. Journal of Geophysical Research: Solid Earth 118, 71–82. https://doi.org/10.1029/2012JB009615

Liu, C., Xu, Q., Shi, B., Deng, S., Zhu, H., 2017. Mechanical properties and energy conversion of 3D close-packed lattice model for brittle rocks. Computers & Geosciences 103, 12–20. https://doi.org/10.1016/j.cageo.2017.03.003

Lu, Y., Chen, X., Wang, L., 2022. Research on fracture mechanism and stability of slope with tensile cracks. Applied Sciences 12, 12687. https://doi.org/10.3390/app122412687

Miao, M., Tang, H., Fang, K., Jiang, Y., Li, C., Lv, B., 2025. Influence of tensile crack development on the deformation behavior and failure mode of reservoir-induced landslides: Insights from model tests. Landslides. https://doi.org/10.1007/s10346-025-02458-2

Michalowski, R.L., 2017. Stability of intact slopes with tensile strength cut-off. Géotechnique 67, 720–727. https://doi.org/10.1680/jgeot.16.p.037

Michalowski, R.L., 2013. Stability assessment of slopes with cracks using limit analysis. Canadian Geotechnical Journal 50, 1011–1021. https://doi.org/10.1139/cgj-2012-0448

Mukhlisin, M., Khiyon, K.N., 2018. The effects of cracking on slope stability. Journal of the Geological Society of India 91, 704–710. https://doi.org/10.1007/s12594-018-0927-5

Park, D., Michalowski, R.L., 2017. Three-dimensional stability analysis of slopes in hard soil/soft rock with tensile strength cut-off. Engineering Geology 229, 73–84. https://doi.org/10.1016/j.enggeo.2017.09.018

Ren, X., Sun, W., Lan, H., Bao, H., Li, L., Liu, S., Yan, C., Wang, X., Li, Z., Tian, C., 2025. Influence of tension cracks on moisture infiltration in loess slopes under high-intensity rainfall conditions. Scientific Reports 15, 4488. https://doi.org/10.1038/s41598-025-88865-w

Saltelli, A., 2002. Making best use of model evaluations to compute sensitivity indices. Computer Physics Communications 145, 280–297. https://doi.org/10.1016/S0010-4655(02)00280-1

Saltelli, A., Annoni, P., Azzini, I., Campolongo, F., Ratto, M., Tarantola, S., 2010. Variance based sensitivity analysis of model output. Design and estimator for the total sensitivity index. Computer Physics Communications 181, 259–270. https://doi.org/10.1016/j.cpc.2009.09.018

Saltelli, A., Ratto, M., Tarantola, S., Campolongo, F., 2006. Sensitivity analysis practices: Strategies for model-based inference. Reliability Engineering & System Safety 91, 1109–1125. https://doi.org/10.1016/j.ress.2005.11.014

Spencer, E., 1968. Effect of tension on the stability of embankments. Journal of the Soil Mechanics and

Foundations Division, ASCE 94 (SM5), 1159–1173.
Stockton, E., Leshchinsky, B.A., Olsen, M.J., Evans, T.M., 2019. Influence of both anisotropic friction and cohesion on the formation of tension cracks and stability of slopes. Engineering Geology 249, 31–44. https://doi.org/10.1016/j.enggeo.2018.12.016
Sun, D., Wang, L., Li, L., 2019. Stability of unsaturated soil slopes with cracks under steady-infiltration conditions. International Journal of Geomechanics 19, 04019044. https://doi.org/10.1061/(asce)gm.1943-5622.0001398
Sun, L., Liu, Q., Abdelaziz, A., Tang, X., Grasselli, G., 2022. Simulating the entire progressive failure process of rock slopes using the combined finite-discrete element method. Computers and Geotechnics 141, 104557. https://doi.org/10.1016/j.compgeo.2021.104557
Taghavi, M., Dovoudi, M.H., Amiri-Tokaldany, E., Darby, S.E., 2010. An analytical method to estimate failure plane angle and tension crack depth for use in riverbank stability analyses. Geomorphology 123, 74–83. https://doi.org/10.1016/j.geomorph.2010.06.017
Tang, L., Zhao, Z., Luo, Z., Sun, Y., 2019. What is the role of tensile cracks in cohesive slopes? Journal of Rock Mechanics and Geotechnical Engineering 11, 314–324. https://doi.org/10.1016/j.jrmge.2018.09.007
Tu, X.B., Kwong, A.K.L., Dai, F.C., Tham, L.G., Min, H., 2009. Field monitoring of rainfall infiltration in a loess slope and analysis of failure mechanism of rainfall-induced landslides. Engineering Geology 105, 134–150. https://doi.org/10.1016/j.enggeo.2008.11.011
Utili, S., 2013. Investigation by limit analysis on the stability of slopes with cracks. Géotechnique 63, 140–154. https://doi.org/10.1680/geot.11.P.068
Venkat Ramana, C., Thote, N.R., Singh, A.K., 2023. Effect of inclined tension crack on rock slope stability by SSR technique. Intelligent Automation & Soft Computing 36, 1205–1214. https://doi.org/10.32604/iasc.2023.031838
Wang, M., Li, D., Tang, X., Liu, Y., 2022. Modeling irregularly inclined fissure surfaces within nonuniform expansive soil slopes. International Journal of Geomechanics 22, 04022124. https://doi.org/10.1061/(asce)gm.1943-5622.0002474
Xian, Y., Wei, X., 2025. Failure mechanism of a snowmelt-related loess landslide group in Ten-zan, China. Geoenvironmental Disasters 12, 30. https://doi.org/10.1186/s40677-025-00334-8
Xu, S., Wang, B., Wang, D., Zhang, J., 2024. A practical stability/instability chart analysis for slope large deformations using the material point method. Engineering Geology 338, 107611. https://doi.org/10.1016/j.enggeo.2024.107611
Yang, X., Sun, X., He, S., Li, Y., 2024. Model test on acoustic emission monitoring of loess slope failure. Sensors 24, 6851. https://doi.org/10.3390/s24216851
Yin, Y., Deng, Q., Li, W., He, K., Wang, Z., Li, H., An, P., Fang, K., 2023. Insight into the crack characteristics and mechanisms of retrogressive slope failures: A large-scale model test. Engineering Geology 327, 107360. https://doi.org/10.1016/j.enggeo.2023.107360
Yuan, W.-H., Liu, K., Zhang, W., Dai, B., Wang, Y., 2020. Dynamic modeling of large deformation slope failure using smoothed particle finite element method. Landslides 17, 1591–1603. https://doi.org/10.1007/s10346-020-01375-w
Zhang, F., Pei, H., 2024. Stability analysis of shallow slopes under rainfall infiltration considering tensile strength cut-off. Computers and Geotechnics 171, 106327. https://doi.org/10.1016/j.compgeo.2024.106327
Zhang, G., Wang, R., Qian, J., Zhang, J., Qian, J., 2012. Effect study of cracks on behavior of soil slope under rainfall conditions. Soils and Foundations 52, 634–643. https://doi.org/10.1016/j.sandf.2012.07.005

Zhang, N., Li, X., Sheng, Z., 2018. A new formula for calculating the depth of trailing-edge tensile cracks in landslides based on the inflection-point principle. Journal of Engineering Geology 26, 157–163. https://doi.org/10.13544/j.cnki.jeg.2018.01.017

Zhao, Z., 2020. Research and assessment on tension cracks and tension-shear coupling failure mode of slope. Doctoral thesis, Sun Yat-sen University.

Zhou, Z., Zhang, J., Ning, F., Luo, Y., Chong, L., Sun, K., 2020. Large-scale test model of the progressive deformation and failure of cracked soil slopes. Journal of Earth Science 31, 1097–1108. https://doi.org/10.1007/s12583-020-1342-6

Zhu, L., Zhou, Z., Chen, L., Xu, T., Zhang, Z., Chen, C., Xu, F., 2021. Limit equilibrium theory-based investigation on the critical tension crack depth in loess slope. Environmental Earth Sciences 80, 349. https://doi.org/10.1007/s12665-021-09641-3